LINEAR STABILITY EXPLORATION OF TRANSCRITICAL NON-ISOTHERMAL POISEUILLE FLOWS

M. BERNADES[1], F. CAPUANO[1] AND L. JOFRE[1]

[1] Department of Fluid Mechanics
Universitat Politècnica de Catalunya · BarcelonaTech (UPC)
Campus Diagonal-Besòs - EEBE, 08019 Barcelona, Spain
e-mail: marc.bernades@upc.edu, www.eebe.upc.edu

Key words: Linear Stability, High-Pressure Transcritical Fluids, Wall-Bounded Non-Isothermal Flows, Laminar-to-Turbulent Transition

Summary. High-pressure transcritical turbulent flow regimes enhance the mixing and heat transfer rates with respect to atmospheric pressure conditions. The two characteristic states of supercritical fluids, gas- and liquid-like, are differentiated across the pseudoboiling line. In this regard, their thermophysical properties in the vicinity of the pseudoboiling region can be leveraged to significantly increase the Reynolds numbers and destabilize the flow. The underlying physical mechanism responsible for this destabilization is the presence of a baroclinic torque, which is formed by the combination of large localized density gradients across the pseudoboiling region (wall-normal direction) and the force driving the flow. As a result, the enstrophy levels are enhanced by approximately $100\times$ compared to equivalent low-pressure cases, and the flow physics behaviour deviates from standard wall-bounded flows. In this work, the nature of this instability is broadly analyzed by means of linear stability theory. It is found that, in isothermal wall-bounded transcritical conditions, the non-linear thermodynamics exhibited near the pseudoboiling region accelerates the turbulence transition with respect to super- and sub-critical states. This transition is further anticipated for non-isothermal flows even at low Brinkman numbers. These effects are here extensively characterized for Poiseuille flows using linear stability analysis. In particular, neutral curve sensitivity to Brinkman numbers and perturbation profiles of dynamic and thermodynamic unstable modes, which trigger the early flow destabilization, are reported in the paper.

1 INTRODUCTION

High-pressure transcritical fluids operate within thermodynamic spaces in which supercritical gas-like and liquid-like states can be differentiated across the pseudoboiling line [1, 2]. As studied by Bernades & Jofre [3], the thermophysical properties of these two regimes in the vicinity of the pseudoboiling region can be leveraged to significantly increase the Reynolds numbers with respect to atmospheric conditions. Among other fields, this result is notably important in microfluidics as it may enable the achievement of microconfined turbulence to obtain enhanced mixing and heat transfer rates. In this regard, the recent direct numerical simulations (DNS) performed by Bernades et al. [4, 5] demonstrated the feasibility of achieving microconfined turbulence by means of utilizing high-pressure transcritical fluids. The resulting flow physics differs significantly from the typical behavior of turbulent wall-bounded flows, due to the presence

of localized baroclinic torques that are responsible for remarkably increasing flow rotation. As a result, the flow becomes unstable and rotation is transformed into a wide range of scales (i.e., turbulent flow motions) through vortex stretching mechanisms. However, the phenomena responsible for destabilizing the flow are still not fully characterized. To this end, this work aims to conduct linear stability analysis of wall-bounded flows at high-pressure transcritical fluid conditions to carefully identify and quantify the underlying flow mechanisms.

Historically, the study of hydrodynamic stability in wall-bounded configurations was first established with incompressible parallel shear flows. In this context, linear stability theory (LST) gave rise to the well-known Orr-Sommerfeld equation [6, 7] and related classical modal results, such as the critical Reynolds number $Re_c = 5772.22$ for plane Poiseuille flow [8, 9] and alternative energy stability-based formulations yielding $Re_c = 49.2$ [10, 11]. Research on the instability of ideal-gas compressible flows started later. Malik et al. [12] introduced LST selecting ρ and T as state variables along with the velocity vector presenting the Jacobian matrices for compressible flows. They characterized the Y-shape spectrum (the so-called branches [13]) and the even and odd modes. Recently, variable viscosity studies such as stratified and Poiseuille flows with temperature dependency have been developed [14, 15] based on a modified set of Orr-Sommerfeld equations, but ignoring the perturbations from temperature and viscosity. Next, Wall [16] investigated the stability effects caused by viscosity. For compressible plane Couette flow, Malik et al. [17] demonstrated that the flow is more stable with viscosity stratification, which was later confirmed by Saikia et al. [18]. Nonetheless, these studies are limited to either incompressible flow or ideal-gas thermodynamics and temperature-dependant transport properties. To this extent, Ren et al. [19] introduced a LST framework for Poiseuille flows for non-ideal fluids. The effects of the dominant dimensionless numbers that characterize the flow, the wall temperature and bulk pressure were analyzed. Results showed that for low Eckert and Prandtl numbers the flow was isothermal, hence a good collapse to incompressible references was observed. Instead, at larger Prandtl and Eckert numbers, the strong gradients of the thermodynamic and transport properties driven by viscous heating became important. In particular, the sub-/trans-/supercritical conditions were compared with respect to ideal-gas scenarios. As a result, the base flow was modally more unstable in the subcritical regime, inviscid unstable in the transcritical regime and significantly more stable in the supercritical regime. To that end, Ren et al. [20] extended these analysis to compressible boundary layers over adiabatic walls with fluids at supercritical pressure. A second co-existing mode was found causing flow destabilization when crossing the pseudoboiling line for two-dimensional perturbations.

The paper is organized as follows. First, in Section 2, the flow physics modeling is presented. Next, the linear stability theory and the linearized equations of supercritical fluids are described. Then, the flow cases are introduced and the linear stability analysis results are presented and discussed in Section 4 for (i) isothermal limit verification, (ii) isothermal and (iii) non-isothermal cases. Finally, Section 5 reports concluding remarks and future directions.

2 FLOW PHYSICS MODELING

The flow motion of supercritical fluids is described by the following set of dimensionless conservation equations of mass, momentum, and total energy

$$\frac{D^\star \rho^\star}{D^\star t^\star} = 0, \tag{1}$$

$$\rho^\star \frac{D^\star \mathbf{u}^\star}{D^\star t^\star} = -\nabla^\star P^\star + \frac{1}{Re} \nabla^\star \cdot \boldsymbol{\tau}^\star + \boldsymbol{F}^\star, \tag{2}$$

$$\rho^\star \frac{D^\star E^\star}{D^\star t^\star} = -\nabla^\star \cdot (P^\star \mathbf{u}^\star) - \frac{1}{ReBr} \nabla^\star \cdot \mathbf{q}^\star + \frac{1}{Re} \nabla^\star \cdot (\boldsymbol{\tau}^\star \cdot \mathbf{u}^\star) + \boldsymbol{F}^\star \cdot \mathbf{u}^\star, \tag{3}$$

where superscript $(\cdot)^\star$ denotes dimensionless quantities, ρ is the density, $\mathbf{u}$ is the velocity vector, P is the pressure, $\boldsymbol{\tau}^\star = \mu^\star(\nabla^\star \mathbf{u}^\star + \nabla^\star \mathbf{u}^{\star T}) - 2/3\mu^\star(\nabla^\star \cdot \mathbf{u}^\star)\boldsymbol{I}$ is the viscous stress tensor, E is the total energy, $\mathbf{q}^\star = -\kappa^\star \nabla^\star T^\star$ is the Fourier heat flux, and $\boldsymbol{F}^\star$ is the normalized body force added to move the fluid.

The resulting set of scaled equations includes two dimensionless numbers: (i) the Reynolds number $Re = \rho_b U_r \delta/\mu_b$, where the subscript b refers to bulk quantities and U_r is the reference streamwise velocity corresponding to its maximum value (i.e., centerline velocity for isothermal conditions), characterizing the ratio between inertial and viscous forces; and (ii) the Brinkman number $Br = \mu_b U_r^2/(\kappa T_b) = PrEc$, where κ is the thermal conductivity, quantifying the ratio of viscous heat generation to external heating through the walls (viz. larger Br values correspond to smaller heat conduction from viscous dissipation resulting in temperature increase). The Brinkman number can also be expressed as the combination of Prandtl number $Pr = \mu_b c_{Pb}/\kappa_b$, where c_P is the isobaric heat capacity, expressing the ratio between momentum and thermal diffusivity, and Eckert number $Ec = U_r^2/(c_{Pb}T_b)$, which accounts for the ratio between advective mass transfer and heat dissipation potential. In this work, the Froude number, which represents the ratio between inertial and gravitational forces, is assumed to be large, and consequently buoyancy effects are not considered. The derivation of these dimensionless equations is based on the following set of inertial-based scalings [21, 22]

$$\mathbf{x}^\star = \frac{\mathbf{x}}{\delta}, \quad \mathbf{u}^\star = \frac{\mathbf{u}}{U_r}, \quad \rho^\star = \frac{\rho}{\rho_b}, \quad T^\star = \frac{T}{T_b}, \quad P^\star = \frac{P}{\rho_b U_r^2},$$

$$E^\star = \frac{E}{U_r^2}, \quad \mu^\star = \frac{\mu}{\mu_b}, \quad \kappa^\star = \frac{\kappa}{\kappa_b}, \quad \boldsymbol{F}^\star = \frac{\boldsymbol{F} U_r \rho_b^2}{\delta}, \tag{4}$$

where $\mathbf{x}$ is position and $D_h = 2\delta$ is the hydraulic diameter, with δ the channel half-height.

The base flow is obtained by solving the Navier-Stokes equations, assuming that the flow is fully developed in a steady laminar state and independent of the streamwise and spanwise directions, i.e., $\partial(\cdot)/\partial x = \partial(\cdot)/\partial z = 0$, $\partial(\cdot)/\partial t = 0$, $v = w = 0$. To this extent, the dimensionless compressible equations of fluid motion (Eqs. 1- 3) are simplified to

$$\frac{d}{dy^\star}\left(\mu^\star \frac{du^\star}{dy^\star}\right) = -ReF^\star = -\hat{F}, \tag{5}$$

$$\frac{dP^\star}{dy^\star} = 0, \tag{6}$$

$$\frac{d}{dy^\star}\left(\frac{\kappa^\star}{Br}\frac{dT^\star}{dy^\star} + \mu^\star u^\star \frac{du^\star}{dy^\star}\right) = -ReF^\star u^\star = -\hat{F}u^\star, \tag{7}$$

3

where density is decoupled from the continuity equation, and therefore depends only on the equation of state. The base flow is fully determined by T, Br and $\hat{F}$. At the isothermal limit ($Br \to 0$), by selecting U_r to be the centerline velocity, results in $\hat{F} = 2$. Thus, the flow is simply governed by $d^2 u^\star / dy^{\star 2} = -\hat{F}$, and consequently $u^\star = y^\star(2 - y^\star)$ is only a function of the distance from the walls. Therefore, without loss of generality, the body force is kept constant, yielding a base flow dependent only on T and Br.

2.1 High-pressure thermophysical properties

The Peng-Robinson equation of state is typically selected to close the thermodynamic state, together with the corresponding thermodynamic potentials based on departure functions [2]. However, this model does not provide the exact reference values from NIST [23], and consequently the CoolProp library [24] is utilized instead. For completeness, the general dimensionless real-gas equation of state can be rewritten as a function of the compressibility factor Z as

$$P^\star = \frac{Z\rho^\star T^\star}{\hat{\gamma}Ma^2},$$
(8)

where $\hat{\gamma} \approx Z(c_P/c_V)[(Z + T(\partial Z/\partial T)_\rho)/(Z + T(\partial Z/\partial T)_P)]$ is an approximated real-gas heat capacity ratio with c_V the isochoric heat capacity. As it can be noted, the dimensionless bulk Mach number $Ma = U_r/c_b$ appears, where c_b is the bulk speed of sound, which represents the ratio of flow velocity to the local speed of sound. Finally, the transport coefficients at high-pressure transcritical conditions are also obtained from the CoolProp library [24].

3 LINEAR STABILITY THEORY

The following subsections describe the linearized stability equations resulting from the base flow model presented above, and the corresponding discretization method utilized to solve them.

3.1 Linearized stability equations

The flow field f can be decomposed into a base flow plus a perturbation (hereafter denoted, respectively, with subscript $(\cdot)_0$ and superscript $(\cdot)'$ yielding the expression $f = f_0 + f'$. The resulting system of equations is composed of 5 variables described by the perturbation vector $\mathbf{q} = (\rho', u', v', w', T')^T$. In this regard, the linear stability equations are derived as a function of the perturbation vector $\mathbf{q}$ substituted in the dimensionless equations of fluid motion (Eqs. 1- 3). The detailed formulae of the resulting linearized equations for real-gas compressible flow can be found in Ren et al. [19]. Particularly, in linear modal stability analysis, the perturbation can be expressed in normal-mode form as

$$\mathbf{q}(x, y, z, t) = \hat{\mathbf{q}}(y) \exp(i\alpha x + i\beta z - i\omega t) + \text{c.c.},$$
(9)

where α and β are the prescribed streamwise and spanwise wavenumber, respectively, ω is the frequency, and c.c. stands for complex conjugate. In particular, Poiseuille flows are inherently dependant on the wall-normal direction and only two-dimensional pertrubations are considered, viz. spanwise wavenumber $\beta = 0$. Consequently, the real and imaginary parts of the eigenvalue ω correspond, respectively, to the wall-normal angular frequency and its local growth rate. Finally, the objective eigenvalue problem is defined based on the temporal operator matrices $\mathbf{A_T}$ and

Table 1: Base flow cases studied utilizing linear stability theory. The first group of cases corresponds to symmetric Poiseuille flows with isothermal walls, whereas the second group considers non-isothermal cases with different cold (cw) and hot (hw) wall temperatures.

Flow case	Regime	Label	T_{cw}/T_c	T_{hw}/T_c	P_b/P_c	Br	Ma
Verification	Superheated steam	V-1	0.95	0.95	1.08	10^{-5}	$4 \cdot 10^{-3}$
Isothermal	High-pressure liquid-like	I-1	0.75	0.75	1.5	$\leq 5 \cdot 10^{-1}$	≤ 0.45
	High-pressure transcritical	I-2	0.95	0.95	1.5	$\leq 5 \cdot 10^{-1}$	≤ 1.37
	High-pressure gas-like	I-3	1.5	1.5	1.5	$\leq 5 \cdot 10^{-1}$	≤ 1.35
Non-isothermal	High-pressure transcritical	NI-1	0.75	1.5	1.5	$\leq 10^{-1}$	≤ 0.33
	High-pressure transcritical	NI-2	0.75	1.5	5	$\leq 10^{-1}$	≤ 0.24
	High-pressure transcritical	NI-3	0.9	1.1	1.5	$\leq 10^{-1}$	≤ 0.44
	Superheated steam	NI-4	0.75	1.5	0.03	$\leq 10^{-1}$	≤ 0.58

$\mathbf{B_T}$ obtained by inspection of expression [19]

$$\mathbf{A_T}\hat{\mathbf{q}} = \omega\mathbf{B_T}\hat{\mathbf{q}}. \tag{10}$$

3.2 Discretization method

The discretization of the linearized equations is based on Chevyshev [25] collocation with a domain constrained between $0 \leq y/\delta \leq 2$, where y is the wall-normal direction of the position vector $\mathbf{x}$ defined as

$$y_j = \delta\left(1 - \cos\frac{\pi j}{N}\right), \quad j = 0, 1, \ldots, N-1, N, \tag{11}$$

where N corresponds to the total number of collocation points. Thus, the Chevyshev differentiation matrices are used to obtain the discretization equations and define the LST eigenvalue problem operators. The mesh size selected for this work is $N = 200$, which provides grid-independent results; for brevity, the corresponding grid-convergence results are not shown in this paper. At larger grid sizes, higher order viscous modes are captured, but the S-shaped Mack branches do not change. Moreover, the system of equations is subjected to $u' = v' = w' = T' = 0$ boundary conditions for both walls.

4 RESULTS

This section describes the flow scenarios studied, and presents and discusses the corresponding results for the isothermal limit verification, isothermal and non-isothermal cases.

4.1 Flow cases studied

The Poiseuille flow considered in this work is set at two different base configurations: (i) *isothermal conditions*, whose base flow is controlled by the Brinkman number, which governs the sub-, trans- and supercritical regimes [19]; and (ii) non-isothermal conditions, where a temperature difference is imposed between the upper and lower walls; in this case, the flow operates within a transcritical regime regardless of the Brinkman number. Consequently, as described in detail in Section 3, the perturbations are solved as an eigenvalue problem ($Re - \alpha$) for the different base flows ($Br - T$) summarized in Table 1.

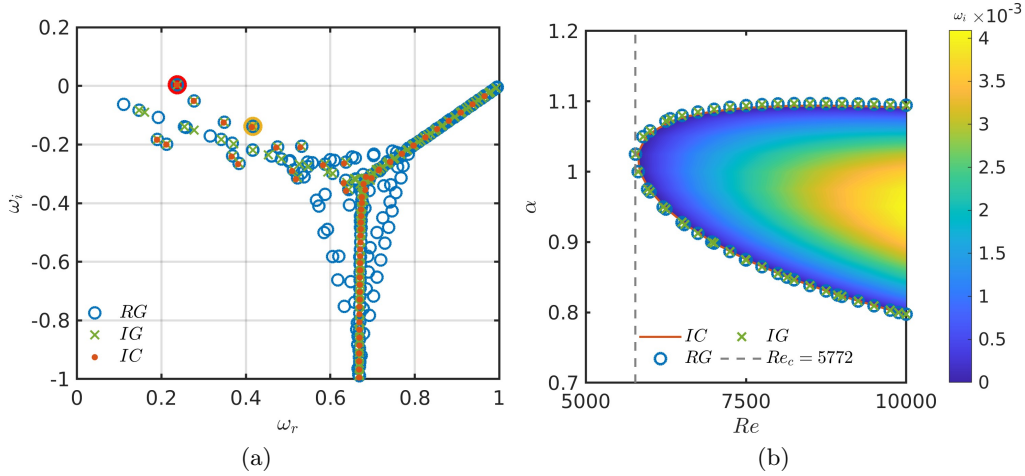Figure 1: (a) Eigenspectrum at $Re = 10000$ and wavenumber $\alpha = 1$, and (b) corresponding neutral curve. Real-gas framework with CoolProp thermophysical properties (RG), ideal-gas model based on power laws (IG), and incompressible framework (IC). In plot (a), the red highlighted eigenvalue corresponds to an unstable mode ($\omega = 0.2375 + 0.0037i$), and the dark-yellow one to a stable mode ($\omega = 0.4164 - 0.1382i$) whose perturbations are depicted in Figure 2.

4.2 Isothermal-limit verification case

The overall approach is preliminarily verified with respect to an incompressible reference solution from Trefethen et al. [26, 25]. To this end, the base flow is obtained from the stability equations at the isothermal limit using CoolProp's real-gas and transport coefficients framework and the ideal-gas model. It is important to note that the perturbations match the results presented by Ren et al. [19] utilizing the REFPROP NIST library [23]. For this comparison, a wall-scaling approach has been used with CO_2 as operating fluid to match the Poiseuille flow conditions from previous verification results [19] at $T_{cw} = T_{hw} = 290\,\mathrm{K}$ and $P = 8\,\mathrm{MPa}$. The spectrum is computed at $Re = 10000$ and wavenumber $\alpha = 1$, and solved for two-dimensional perturbations, i.e., $\beta = 0$. Figure 1 depicts the corresponding (a) eigenspectrum and (b) neutral curve. It can be observed that Mack branches [13], the so-called A-, P- and S-branches, are properly reproduced by the incompressible flow case. At the isothermal limit, the ideal-gas model collapses to these branches. However, the real-gas framework solution introduces additional modes due to thermophysical effects, i.e., modes driven by thermophysical phenomena (density and temperature perturbations). Nonetheless, the same unstable mode is captured by the frameworks considered as it is a dynamic mode independent of thermodynamic effects. Moreover, the neutral curve shows good agreement between the different models considered, and in particular they all yield the classical result $Re_c = 5772$. Finally, Figure 2 contains the perturbations of (a) the unstable mode and (b) the stable mode [dark-yellow eigenvalue in Figure 1 (a)]. It has been verified that, while the unstable modes between real- and ideal-gas frameworks are identical, small differences emerge for the stable mode, which correspond to compressibility effects related to the density perturbation, and are only captured by real-gas thermodynamics as shown in the inset of Figure 2(b).
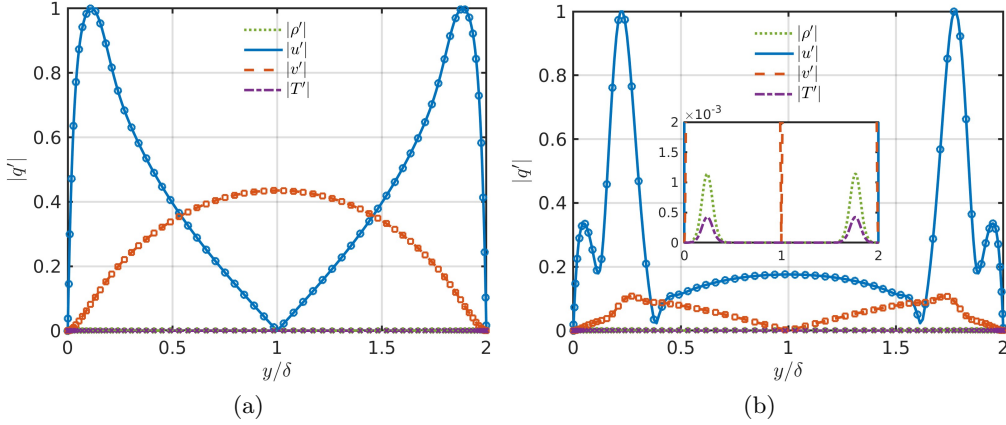
6

Figure 2: Perturbation profiles of (a) unstable ($\omega = 0.2375 + 0.0037i$) and (b) stable ($\omega = 0.4164 - 0.1382i$) modes normalized by $|u'|$. Real-gas framework with CoolProp thermophysical properties (RG) (solid lines), and ideal-gas model with power laws (IG) (markers).

4.3 Isothermal cases

Figure 3 depicts the neutral curves for the isothermal cases (labeled I-1, I-2 and I-3 in Table 1). It is known that the larger Br the larger the base flow centerline velocity and temperature. First, the I-1 subcritical regime case (centerline temperature below T_c) yields a reduced stability region with respect to the isothermal limit when Br increases. In particular, the neutral curve expands to lower Re for a wider range of wavenumbers, and becomes unstable at $Re_c \approx 1000$ (refer to Table 2) at $1.0 \lesssim \alpha \lesssim 1.2$. Next, the I-2 base flow undergoes a transcritical trajectory across the pseudoboiling region, and as a result both velocity and temperature become inflectional at $Br \gtrsim 0.35$. This results in a lower $Re_c \approx 500$ (refer to Table 2) and a significantly wider range of wavenumbers, $1.2 \lesssim \alpha \lesssim 1.7$, where early laminar to turbulent transition can occur. Third, the I-3 case operates at supercritical conditions behaving similarly as the ideal-gas solution [19], in which increasing Br enhances the stability region. In particular, for $Br > 0.05$ the flow is stable for the $Re - \alpha$ parameter space analyzed.

To this extent, Figure 4 shows the perturbations of the most unstable region, i.e., $Re = 10^4$ and $\alpha = 1$. The subcritical regimes are dominated by density and temperature perturbations (thermophysical-driven mode), unlike for the isothermal limit. Its effect is, however, diminished at larger Br. At transcritical conditions, velocity perturbations dominate towards the walls along with temperature and density with lower magnitude. The vertical velocity governs the flow instability at the center. Instead, supercritical flow destabilization is only dominated by streamwise velocity (dynamic-driven mode).

4.4 Non-isothermal cases

Figure 5 depicts the neutral curves for the non-isothermal cases. It is noted that in this case the the fluid is forced to cross the pseudoboiling line for all Br. Consequently, this yields lower velocities. In fact, the Br top-end is limited so that temperature remains below the hot wall temperature, which corresponds to $Br \leq 0.1$. While NI-1 and NI-3 are crossing the pseudoboiling region, NI-2 is pressurized much beyond the critical pressure and consequently it operates at
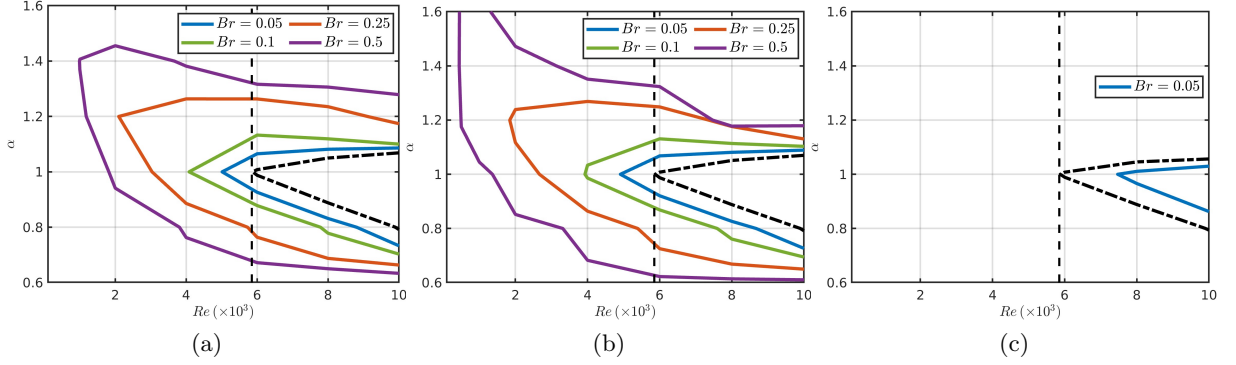
Figure 3: Neutral curves for various Br at (a) sub-, (b) trans- and (c) supercritical regimes. Dashed-dotted line represents the isothermal limit ($Br \to 0$), and the vertical dashed line denotes $Re_c = 5772$.
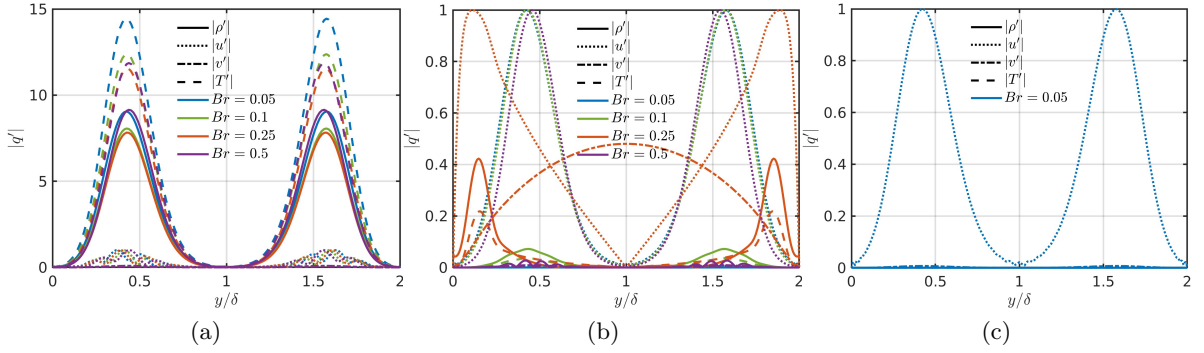

Figure 4: Perturbation profiles of the most unstable mode at $Re = 10000$, $\alpha = 1$ along the wall-normal direction for various Br numbers at (a) sub-, (b) trans- and (c) supercritical regimes.
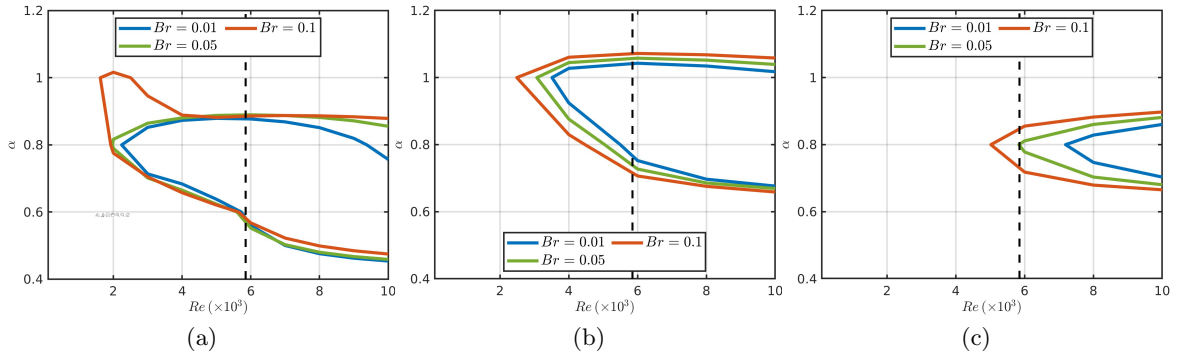

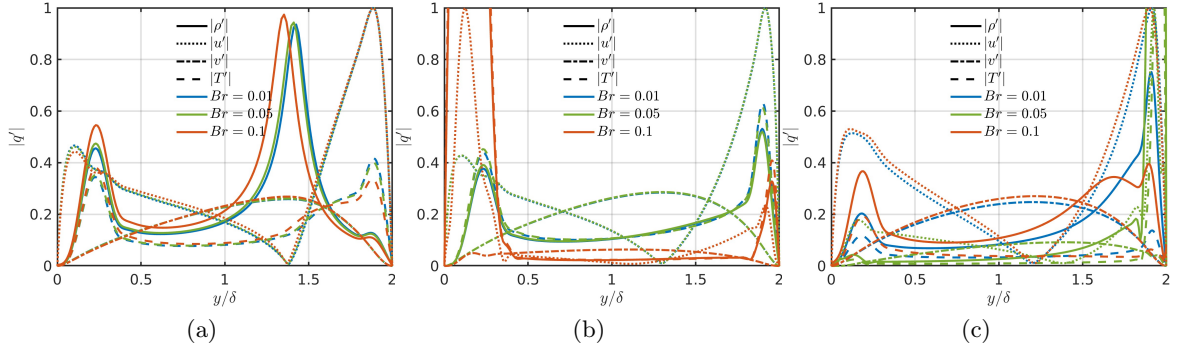Figure 5: Neutral curves for various Br for (a) $NI - 1$, (b) $NI - 2$, and (c) $NI - 3$ cases.

8

Figure 6: Perturbation profiles of the most unstable mode at $Re = 10000$ along the wall-normal direction for various Br: (a) $NI - 1$ ($\alpha = 0.8$), (b) $NI - 2$ ($\alpha = 1$), (c) $NI - 3$ ($\alpha = 0.8$) cases.
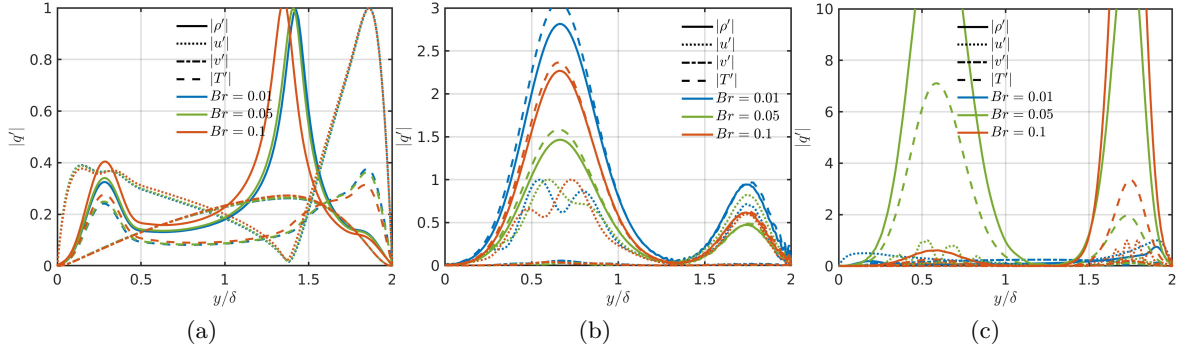

Figure 7: Perturbation profiles of the most unstable mode for (a) $NI - 1$ at $Re = 4000$ and $\alpha = 0.8$, (b) $NI - 2$ at $Re = 4000$ and $\alpha = 1$, and (c) $NI - 3$ at $Re = 8000$ and $\alpha = 0.8$.

supercritical conditions. The neutral curves of NI-1 are similar for all Br, where the instability is biased towards lower Re; especially compared to low Br numbers from the isothermal cases. In addition, the wavenumber of Re_c falls $\sim 20\%$. Nevertheless, NI-3 results in larger Re_c, even beyond the isothermal limit transition when $Br < 0.05$. Therefore, by constraining the cold and hot temperatures closer to the critical point, the stability region is enhanced with respect to wider operating temperature windows, as in NI-1. Finally, when increasing the pressure of the system, the neutral curves display similar envelopes as in the subcritical isothermal case.

Analogously, Figure 6 presents the perturbation profile of the most unstable modes at the largest analyzed Re. The perturbations are dominated by density and temperature near the pseudoboiling region, but velocity is significantly high near the hot wall. The cold wall thermodynamics and streamwise velocity have similar magnitudes, although they are 50% lower than at the hot wall. This behaviour is similar for both transcritical cases, NI-1 and NI-3, with small differences among Br numbers. Instead, NI-2 is mainly dominated by streamwise velocity near the walls and vertical velocity at the center. Although at large Br the cold wall density and temperature perturbations become greater than the streamwise velocity. Additionally, the perturbations near the Re_c value are depicted in Figure 7. NI-1 perturbations are similar to larger Re. However, for NI-2 are dominated by thermodynamics at $y/\delta \sim 0.75$ and $y/\delta \sim 1.75$

by a factor $3\times$ with respect to velocity perturbation, whereas NI-3 is clearly dominated by thermodynamic modes at both peak locations. Finally, the NI-4 case operates at low-pressure conditions and stability results collapse to the ideal-gas solution. Nonetheless, although it operates at different temperatures, the system is stable for all Reynolds numbers and wavenumbers considered.

4.5   Laminar-to-turbulent transition summary

The critical Reynolds numbers of each case from the neutral curves are summarized in Table 2.

Table 2: Critical Reynolds numbers for the flow cases described in Section 4.1.

Br	V-1	I-1	I-2	I-3	NI-1	NI-2	NI-3	NI-4
$Br \rightarrow 0$	5844		5875		$-$	$-$	$-$	$-$
0.01		5631	5610	6056	2240	3510	7190	$> 10^4$
0.05		5013	4910	7468	1975	3069	5833	$> 10^4$
0.10	$-$	4080	3927	$> 10^4$	1618	2486	5019	$> 10^4$
0.25		2096	1842	$> 10^4$	$-$	$-$	$-$	$-$
0.50		990	441	$> 10^4$	$-$	$-$	$-$	$-$

5   CONCLUSIONS

A high-pressure real-gas flow framework for linear stability analysis of plane Poiseuille flows has been presented. The approach has been verified at the isothermal limit and shown to recover the reference results from incompressible Poiseuille flow. The exploratory analysis presented in this work focused on streamwise perturbations for iso- and non-isothermal cases for various Brinkman numbers. The results showed that, for isothermal cases, the destabilization occurs at lower Re when Br increases for sub- and transcritical flows. In particular, under transcritical conditions, the transition from laminar to turbulence occurs at lower Re than for subcritical flows. Instead, the supercritical cases result in stability enhancement when Br increases, similarly to ideal-gas cases. Alternatively, non-isothermal conditions were assessed by enforcing the fluid to operate across the pseudoboiling region. Therefore, transcritical conditions are achieved at lower Br than isothermal cases. Consequently, destabilization effects are observed at relatively lower Br, with small differences among the Br base flows. To this end, the asymmetric setups are attractive to accelerate turbulence transition at lower bulk velocities.

In detail, for the isothermal transcritical case, the Re_c is $5\times$ lower than for the isothermal limit case for a wide range of wavenumbers. Instead, for the same Br number at subcritical conditions, the neutral curve is shifted $2\times$ with respect to the transcritical regime. In fact, density and temperature perturbations are mostly responsible for such destabilization for both regimes. However, supercritical regimes enhance the stability if Br increases and the perturbations are driven by streamwise velocity. Furthermore, non-isothermal setups result in flow destabilisation at lower Br and 20% wavenumber reduction than the isothermal cases. It is important to note that, by increasing the pressure of the system by $5\times$, the critical point recovers similar neutral curves as in the isothermal subcritical case, but still at lower Re_c. However, if the asymmetric temperature difference is reduced, the laminar to turbulent transition becomes limited and comparable Re_c values as in the isothermal subcritical case are obtained. The perturbations are

dominated by the thermodynamic modes, especially near the pseudoboiling region.

As future work, extension of the analysis of the non-isothermal cases will be further characterized, in particular, the energy budgets and growth rates comparing both iso- and non-isothermal setups. Consequently, the unstable modes with 2D perturbations will also be investigated to evaluate the presence of additional modes for the transcritical case, which are non-existing in subcritical and supercritical regimes. In addition, DNS baseflow will be computed and destabilized by superimposing the most unstable modes to validate the LST results.

ACKNOWLEDGMENTS

References

[1] L. Jofre and J. Urzay. A characteristic length scale for density gradients in supercritical monocomponent flows near pseudoboiling. *Annual Research Briefs, Center for Turbulence Research, Stanford University*, pages 277–282, 2020.

[2] L. Jofre and J. Urzay. Transcritical diffuse-interface hydrodynamics of propellants in high-pressure combustors of chemical propulsion systems. *Prog. Energy Combust. Sci.*, 82:100877, 2021.

[3] M. Bernades and L. Jofre. Thermophysical analysis of microconfined turbulent flow regimes at supercritical fluid conditions in heat transfer applications. *J. Heat Transfer*, 144:082501, 2022.

[4] M. Bernades, F. Capuano, F. X. Trias, and L. Jofre. Energy-preserving stable computations of high-pressure supercritical fluids turbulence. In *8th ECCOMAS*, pages 1–12, 2022.

[5] M. Bernades, F. Capuano, and L. Jofre. Microconfined high-pressure transcritical fluid turbulence. *Phys. Fluids*, 35:015163, 2023.

[6] William M'F. Orr. *The Stability or Instability of the Steady Motions of a Perfect Liquid and of a Viscous Liquid. Part II: A Viscous Liquid*, volume 27. Royal Irish Academy, 1907.

[7] A. Sommerfeld. Ein beitrag zur hydrodynamischen erklarung der turbulenten flussigkeisbewegung. In *Atti Congr. Int. Math. 4th Rome*, pages 116–124. Academia dei Lincei, 1908.

[8] L. H. Thomas. The stability of plane poiseuille flow. *Phys. Rev.*, 91(4):780–783, 1953.

[9] S. A. Orzag. Accurate solution of the orr–sommerfeld stability equation. *J. Fluid Mech.*, 50:689–703, 1971.

[10] F. H. Busse. Bounds on the transport of mass and momentum by turbulent flow between parallel platesw. *Z. Angew. Math. Phys.*, 20(1):1–14, 1969.

[11] D. D Joseph and S Carmi. Stability of poiseuille flow in pipes, annuli, and channels. *Q Appl Math.*, 26(4):575–599, 1969.

[12] M. Malik, M. Alam, and J. Dey. Nonmodal energy growth and optimal perturbations in compressible plane couette flow. *Phys. Fluids*, 18:034103, 2006.

[13] L. M. Mack. A numerical study of the temporal eigenvalue spectrum of the blasius boundary layer. *J. Fluid Mech.*, 73(3):497–520, 1976.

[14] R. Govindarajan and K. C. Sahu. Instabilities in viscosity-stratified flow. *Annu. Rev. Fluid Mech.*, 46(1):331–353, 2014.

[15] M. C. Potter and E. Graber. Estability of plane poiseuille flow with heat transfer. *Phys. Fluids*, 15(3):387–391, 1972.

[16] W. Wall. The linear stability of channel flow of fluid with temperature-dependent viscosity. *J. Fluid Mech.*, 323:107–132, 1996.

[17] M. Malik, J. Dey, and M. Alam. Linear stability, transient energy growth, and the role of viscosity stratification in compressible plane couette flow. *Phys. Rev. E*, 77(3):036322, 2008.

[18] B. Saikia, A. Ramachandran, K. Sinha, and R. Govindarajan. Effects of viscosity and conductivity stratification on the linear stability and transient growth within compressible couette flow. *Phys. Fluids*, 29(2):024105, 2017.

[19] J. Ren, O. Marxen, and R. Pecnik. Boundary-layer stability of supercritical fluids in the vicinity of the Widom line. *J. Fluid Mech.*, 871:831–864, 2019.

[20] J. Ren, S. Fu, and R. Pecnik. Linear instability of poiseuille flows with highly non-ideal fluids. *J. Fluid Mech.*, 859:89–125, 2019.

[21] L. Jofre, Z. R. del Rosario, and G. Iaccarino. Data-driven dimensional analysis of heat transfer in irradiated particle-laden turbulent flow. *Int. J. Multiph. Fl.*, 125:103198, 2020.

[22] L. Jofre, M. Bernades, and F. Capuano. Dimensionality reduction of non-buoyant micro-confined high-pressure transcritical fluid turbulence. *Int. J. Heat Fluid Flow*, 102:109169, 2023.

[23] P. J. Linstrom and W. G. Mallard. Thermophysical properties of fluid systems, NIST Chemistry Webbook (SRD 69), 2021.

[24] I. H. Bell, J. Wronski, S. Quoilin, and V. Lemort. Pure and pseudo-pure fluid thermophysical property evaluation and the open-source thermophysical property library coolprop. *Ind. Eng. Chem. Res.*, 53(6):2498–2508, 2014.

[25] L. N. Trefethen. *Spectral Methods in MATLAB*. Society for Industrial and Applied Mathematics, 2000.

[26] L. N. Trefethen, A. E. Trefethen, S. C. Reddy, and T. A. Driscoll. Hydrodynamic stability without eigenvalues. *Science*, 261(5121):578–584, 1993.